imageOwl

TOTAL QA®
Turn Complex to Complete

Improve your test life.

Imagine if you had an integrated QA system that works for you...

Our clients start with an incoherent mix of isolated QA devices, checklists, forms, image processing software, and spreadsheets. As they try to integrate their QA, they are frustrated by systems that won't adapt to their needs.

With Total QA®, they discover a clinically tested, powerful, and customizable service that transforms their machine QA into a coherent whole. With built-in image analysis, custom test templates and a complete API, our clients build QA systems to meet their unique mix of equipment and procedures.

You can improve your test life.
Request a free trial and try it for 3 months free!

Challenges in MR-only seed localization for postimplant dosimetry in permanent prostate brachytherapy

Frank Zijlstra[a)]
Image Sciences Institute, University Medical Center Utrecht, Utrecht, The Netherlands

Marinus A. Moerland, Jochem R.N. van der Voort van Zyp, and Juus L. Noteboom
Department of Radiotherapy, University Medical Center Utrecht, Utrecht, The Netherlands

Max A. Viergever and Peter R. Seevinck
Image Sciences Institute, University Medical Center Utrecht, Utrecht, The Netherlands

(Received 18 April 2017; revised 17 July 2017; accepted for publication 22 July 2017; published 11 September 2017)

Purpose: An MR-only postimplant dosimetry workflow for low dose rate (LDR) brachytherapy could reduce patient burden, improve accuracy, and improve cost efficiency. However, localization of brachytherapy seeds on MRI scans remains a major challenge for this type of workflow. In this study, we propose and validate an MR-only seed localization method and identify remaining challenges.
Methods and materials: The localization method was based on template matching of simulations of complex-valued imaging artifacts around metal brachytherapy seeds. The method was applied to MRI scans of 25 prostate cancer patients who underwent LDR brachytherapy and for whom postimplant dosimetry was performed after 4 weeks. The seed locations found with the MR-only method were validated against the seed locations found on CT. The circumstances in which detection errors were made were classified to gain an insight in the nature of the errors.
Results: A total of 1490 of 1557 (96%) seeds were correctly detected, while 67 false-positive errors were made. The correctly detected seed locations had a high spatial accuracy with an average error of 0.8 mm compared with CT. A majority of the false positives occurred near other seeds. Most false negatives were found in either stranded configurations without spacers or near other seeds.
Conclusions: The low detection error rate and high localization accuracy obtained by the complex-valued template matching approach are promising for future clinical application of MR-only dosimetry. The most important remaining challenge is robustness with regard to configurations of multiple seeds in close vicinity, such as in strands of seeds without spacers. This issue could potentially be resolved by simulating specific configurations of multiple seeds or by constraining the treatment planning to avoid these configurations, which could make the proposed method competitive with CT-based seed localization. © *2017 The Authors Medical Physics published by Wiley Periodicals, Inc. on behalf of American Association of Physicists in Medicine.* [https://doi.org/10.1002/mp.12505]

Key words: brachytherapy, MRI, seed localization, simulation, susceptibility, template matching

1. INTRODUCTION

Postimplant dosimetry is an important tool for quality assurance after low dose rate (LDR) prostate brachytherapy. Despite various innovations in planning and delivery of brachytherapy seeds,[1–3] the actual dose distribution may deviate from the planned distribution due to errors in needle positioning, errors in seed delivery, prostate deformation between needle insertion and retraction, edema, and seed migration.[1,4,5] Therefore, postimplant dosimetry is recommended to assure the quality of the implant workflow and to establish accurate dose–response relationships.[6]

In current practice for postimplant dosimetry, CT is the modality of choice for localizing brachytherapy seeds on account of its high sensitivity to the metal components in the brachytherapy seeds.[1,6] However, delineation of the prostate and the organs at risk around the prostate is challenging because of the low contrast in soft tissues in CT images.[7] MR images, however, provide excellent soft tissue contrast and are often used for delineation of the prostate, tumor, and organs at risk.[8,9] These delineations are then registered to CT images to perform high-quality dosimetry,[10,11] although uncertainties in delineation and image registration may impair accuracy of postimplant dosimetry. Furthermore, a disadvantage of the use of image registration is that errors may occur because of deformation of the prostate in between the CT and MRI scans, which may be caused by changes in patient position, or by physiological factors such as changes in bladder and rectum filling.

An MR-only approach to postimplant dosimetry could remove registration as a source of errors by providing intrinsically registered seed localization and organ delineations. Furthermore, patient burden and costs would be reduced by the omission of CT scanning in the workflow.[12] However, although MR-only approaches for localizing brachytherapy seeds have been investigated by several groups,[13–19] no method has proven robust and accurate enough for clinical use as yet.

© 2017 The Authors Medical Physics published by Wiley Periodicals, Inc. on behalf of American Association of Physicists in Medicine. This is an open access article under the terms of the Creative Commons Attribution-NonCommercial License, which permits use, distribution and reproduction in any medium, provided the original work is properly cited and is not used for commercial purposes.

Some studies have only considered the susceptibility-induced signal voids caused by brachytherapy seeds in MRI.[13–15] A problem with this approach is that signal voids are not specific to brachytherapy seeds. Other sources of signal voids in the prostate include vessels, small bleeds, and calcifications.

Further studies have solved this issue by focusing on the off-resonance effects around brachytherapy seeds. Kuo et al. describe the use of the IRON (inversion recovery with on-resonant water suppression) prepulse for suppressing on-resonant signal, which creates positive contrast at the off-resonant signal around brachytherapy seeds.[16] A disadvantage of this method is that it is also sensitive to other sources of field inhomogeneity, which does not make it robust for *in vivo* application. The co-RASOR (center-out radial sampling with off-resonance reception) method was proposed to shift local signal pile-ups caused by off-resonance back to the center of the brachytherapy seed in radial acquisitions.[19] Dong et al. applied susceptibility gradient mapping to specifically use the local dephasing around brachytherapy seeds to generate positive contrast at the location of the seed.[17] Since these two approaches are based on local susceptibility effects, they are less sensitive to other field inhomogeneities.

A problem that remains with all of these methods is that generating positive contrast in itself is not enough for accurate localization of brachytherapy seeds. A robust detection algorithm would still be required to localize the seeds in varying orientations and in varying configurations.

Wachowicz et al. have proposed the use of simulations to characterize the artifacts around brachytherapy seeds and subsequently using these simulated images to establish the location and orientation of the seed in an experimentally obtained image.[18] For a large number of possible orientations of a seed, they performed an MRI simulation, which were matched to the image using normalized cross-correlation. Although the method was only demonstrated for a 2D spin echo sequence, the approach can theoretically be applied to any sequence, as long as accurate simulations for that sequence can be performed in reasonable time.

In this study, we have investigated the potential and challenges of an MR-only brachytherapy seed localization method using a comprehensive dataset of 25 prostate cancer patients who underwent LDR brachytherapy. We used a seed localization methodology that improves on the method proposed by Wachowicz et al. by incorporating complex-valued 3D MR simulations, provided by a recently proposed method for efficiently simulating off-resonance artifacts in steady-state gradient echo MRI sequences.[20] The resulting method is applicable to 3D images and exploits the off-resonance artifacts present in both the magnitude and the phase of the MR images to determine the location and orientation of multiple brachytherapy seeds. The localization results were verified against clinically used seed detections based on CT images, and all detection errors were examined to determine the circumstances in which the errors occurred. Based on the results, we identify remaining challenges for applying MR-only postimplant dosimetry in clinical practice.

2. METHODS

2.A. Patients

For this study, we recruited 25 prostate cancer patients who underwent LDR prostate brachytherapy between February 2015 and May 2016 and gave informed consent for an additional MRI scan optimized for MR-only seed detection. Informed consent was obtained in accordance to the guidelines of the Institutional Review Board of the University Medical Center Utrecht. A total of 17 patients were treated using Best medical model 2301 (Best Medical Inc, Springfield, USA) I-125 seeds [Fig. 1(a), top], with an average number of seeds implanted of 62 ± 7 [mean $\pm$ standard deviation

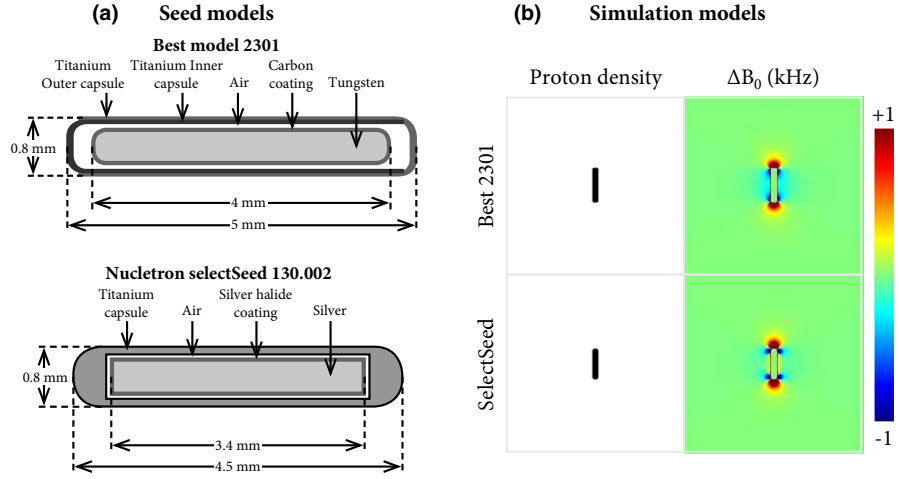

FIG. 1. (a) Schematics of the Best model 2301 (top) and Nucletron selectSeed 130.002 (bottom) brachytherapy seeds with material types indicated. (b) Proton density and ΔB_0 maps that were used to simulate a seed-oriented parallel with B_0. The maps were generated at a resolution of 0.075 mm and cover a field of view of $25 \times 25 \times 25$ mm. [Color figure can be viewed at wileyonlinelibrary.com]

(SD)]. The remaining eight patients were treated using Nucletron selectSeed model 130.002 (Elekta/Nucletron, Veenendaal, The Netherlands) I-125 seeds [Fig. 1(a), bottom], with an average number of seeds implanted of 64 ± 16 (mean $\pm$ SD). Most seeds were implanted in stranded configurations, optionally spaced with 5-mm plastic spacers. If no spacers were used, we refer to those strands as unspaced strands. Best 2301 seeds in stranded configurations were always physically attached to the spacers or to other seeds. In contrast, the selectSeed seeds were never physically attached to either seeds or spacers.

Regular clinical postimplant dosimetry was performed around 4 weeks after implantation using a CT- and MRI-based approach. Semi-automatically detected seed locations were obtained from CT scans using the treatment planning system Oncentra Prostate (Elekta/Nucletron, Veenendaal, The Netherlands). This served as the gold standard in the validation of our proposed MR-only seed localization approach.

A 3D gradient echo scan was included in the regular MRI scanning protocol to facilitate the MR-only seed localization proposed in this study. Relevant scan parameters were 1.2 mm isotropic acquired resolution, matrix size $292 \times 376 \times 75$, field of view $350 \times 451 \times 90$ mm, TE/TR 2.7/4.6 ms, readout direction = anterior–posterior, readout bandwidth = ~1155 Hz/pixel, flip angle 10°, and a scan time of 130 s. To prevent motion artifacts due to breathing from spilling into the prostate region, we chose the readout direction in the anterior–posterior direction, because the readout direction is less susceptible to motion artifacts. Scans were acquired at 3 tesla (Ingenia, Philips Healthcare, Best, The Netherlands) using a 32 channel torso coil. Figure 2 shows an example of this scan for a patient treated with Best 2301 seeds.

2.B. Seed localization

We improved on the methodology proposed by Wachowicz et al. in a number of ways. First, we changed the simulation method to allow simulation of 3D gradient echo MRI scans, instead of only 2D spin echo scans. Second, we modified the template matching from using normalized cross-correlation to phase correlation,[21] which appeared more robust with respect to background signal variations that are present *in vivo*. And finally, to aid in the detection of the large number of seeds present, we introduced additional steps to eliminate false-positive detections.

2.C. Library generation

To simulate complex-valued artifacts around brachytherapy seeds in high resolution for 3D gradient echo scans in reasonable time, we used the FORECAST (Fourier-based Off-REsonanCe Artifact simulation in the STeady-state) method.[20] The simulated artifacts include spatial distortion, dephasing, and signal dropout due to intra-voxel dephasing. The simulation models were generated at a resolution of 0.075 mm in a $25 \times 25 \times 25$ mm region around a brachytherapy seed. The models contained the brachytherapy seed in a uniform medium with proton density set to 1 and a T_2 value of 50 ms. Based on magnetic susceptibility models of the brachytherapy seeds [Fig. 1(a)], we calculated ΔB_0 maps for both seed models using a fast method for field-shift calculation[22] [Fig. 1(b)]. Figure 3(a) shows an example of the scanned and simulated complex-valued artifacts for each seed type. We simulated a library of 321 seed orientations for each of the two types of brachytherapy seeds. The seed orientations were sampled approximately uniformly as orientation vectors positioned on a half-sphere. Figure 3(b) shows how the complex-valued artifacts vary with seed orientation for a subset of the simulated libraries.

2.D. Template matching

In initial experiments, we found that the normalized cross-correlation used by Wachowicz et al. was not robust against signal variations that were present *in vivo*. For this reason, we used the phase correlation method[21] to perform template matching of the libraries with an acquired MRI scan in the frequency domain. Phase correlation is mathematically defined as the following elementwise operation in the frequency domain:

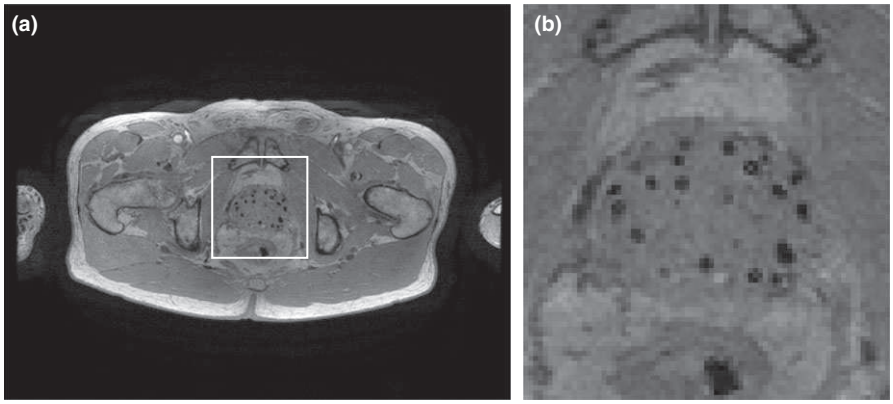

FIG. 2. A magnitude image of a transverse slice of the 3D gradient echo scan that was used for seed localization (a), and an enlarged region around the prostate in which Best medical model 2301 brachytherapy seeds are present (b). The region is indicated by the white box in A.

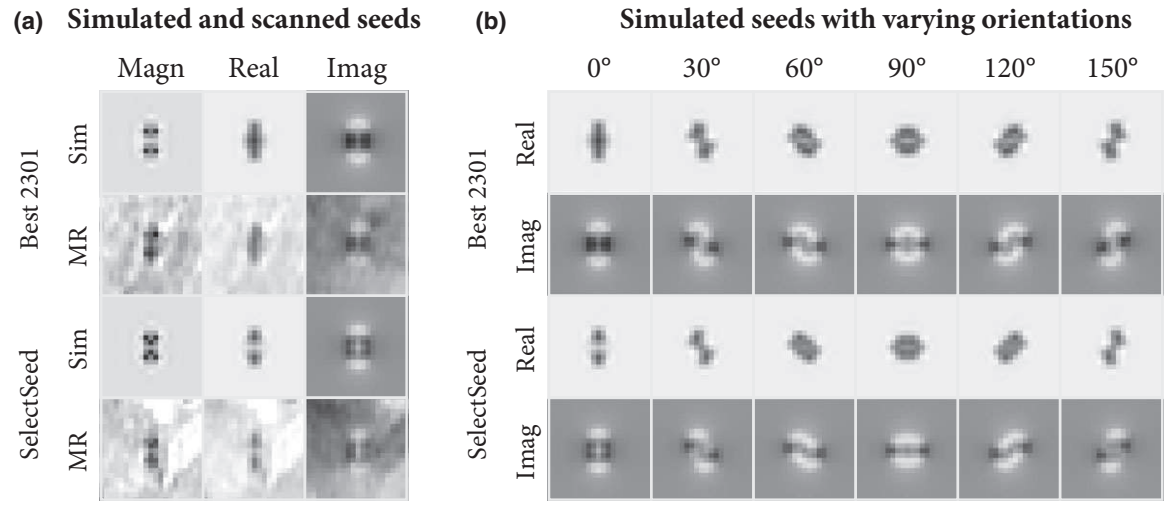

FIG. 3. (a) Coronal slice of MR simulations (Sim) and *in vivo* images (MR) for a seed oriented parallel with B_0 for a Best 2301 (top) and a SelectSeed (bottom) seed. Both the magnitude (Magn) and the real and imaginary (Imag) components are shown. (b) A subset of the simulated template libraries for varying orientations of the seeds. The images show the complex components (Real/Imag) of the simulations for rotations in the coronal plane with steps of 30°.

$$C(\boldsymbol{k}) = \frac{I(\boldsymbol{k})\overline{T(\boldsymbol{k})}}{|I(\boldsymbol{k})\overline{T(\boldsymbol{k})}| + \varepsilon}$$

Here, I is the frequency domain of the MR image, $\overline{T}$ is the complex conjugate of the frequency domain of the simulated template image, C is the frequency domain of the phase correlation image, $\boldsymbol{k}$ is the location of the frequency domain element to which the operation is applied, and ε is a constant that prevents division by zero, which was set to 10^{-15}. The phase correlation in the spatial domain is then obtained by performing an inverse fast Fourier transform on C. This is repeated for each template in the library. For each voxel in the scan, the template with the highest correlation was determined and stored as a candidate seed detection. We applied the template matching in a cubical region of interest incorporating the prostate with a margin of 5 mm between the delineated prostate and the bounding box.

2.E. Seed detection

In order to reduce the number of false-positive detections, we selected 1000 candidate detections with the highest correlations. On each of these candidates, we performed a local linear regression of the measured signal around the candidate to the matched template to determine how well the template fit to the local signal. At the location of the candidate detection, the matched template was placed over the MR image to allow a voxelwise comparison of image and template intensities. All voxels in the template that deviated at least 20% from the background intensity (i.e., where artifacts were present) were used to solve the following linear regression problem:

$$aI(\boldsymbol{r}) + b = T(\boldsymbol{r})$$

Here, I is the complex MR image intensity at location $\boldsymbol{r}$, T is the complex template image intensity at location $\boldsymbol{r}$, and a and b are the complex-valued coefficients fitted using linear regression, which minimizes the sum of squared residual errors:

$$\sum_{\boldsymbol{r}} |aI(\boldsymbol{r}) + b - T(\boldsymbol{r})|^2$$

We will refer to this sum as the residual error after linear regression, which indicates how well a template matched the local signal around a candidate seed detection.

Next, candidates were accepted in the order of their residual error, starting with the candidates with the lowest errors. For each accepted candidate, the dephasing caused by the presence of the seed was corrected by unwinding the phase in the image as predicted by the best matching template at that location (Fig. 4, last column). For every voxel in the template, the following phase correction was applied:

$$I_{new}(\boldsymbol{r}) = I(\boldsymbol{r})e^{-i\,Arg(T(\boldsymbol{r}))}$$

Here, I_{new} is the complex MR image intensity after phase unwinding, and $Arg(T(\boldsymbol{r}))$ is the complex argument (i.e., the phase) of the template at location **r**.

After each phase correction, the local regression was recalculated for each candidate affected by the correction. Furthermore, all candidates within 1 voxel distance of the accepted detection were removed to prevent multiple detections of a single seed. This detection process was repeated until the number of detected seeds was equal to the number of implanted seeds.

2.F. Experimental setup

We applied our MR-only seed detection to each of the 25 subjects, using the specific library for the type of seed that was implanted. In order to compare the detected seed locations found on MRI to the detected seed locations on CT, we performed a rigid registration of the two point sets using the Coherent Point Drift method.[23] Next, an automatic matching was applied to find matching pairs of detections on MRI and

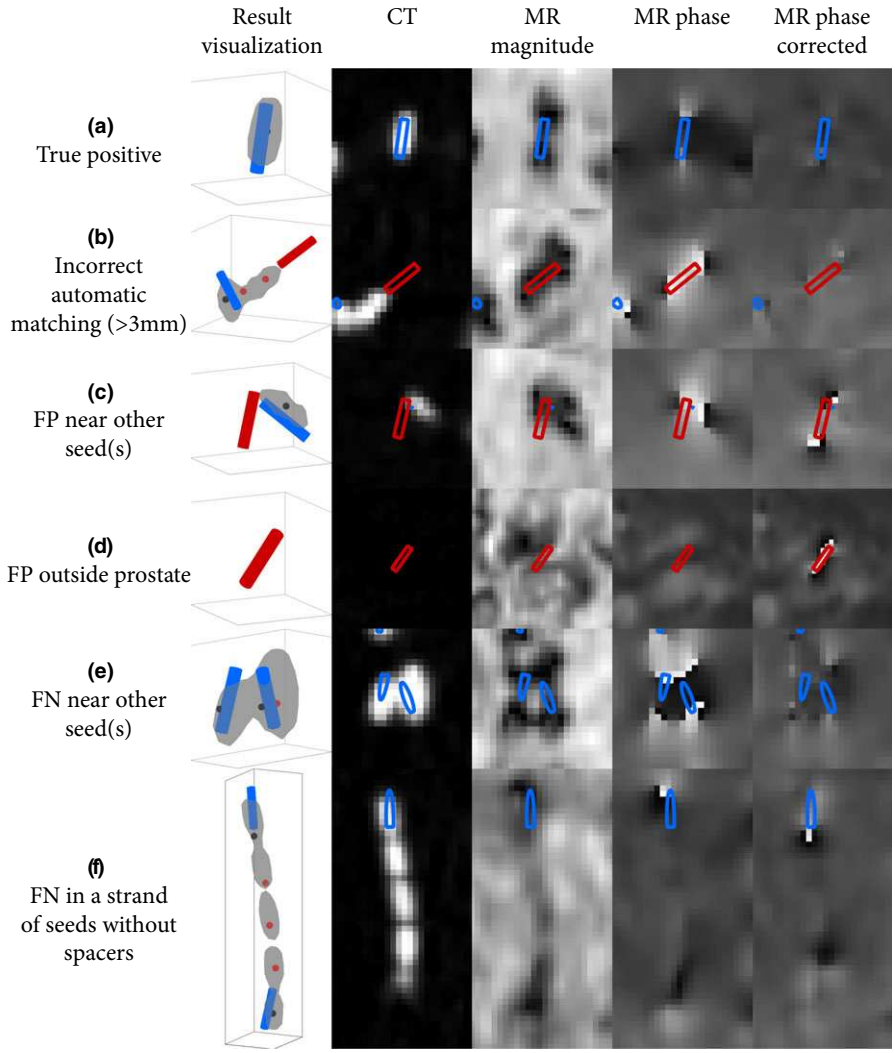

FIG. 4. Examples of the conditions in which classification errors [false positive (FP) and false negative (FN)] occurred. For reference, A shows a true positive (TP) detection. In the first column, a rendering of the detected seeds (blue cylinder = TP, red cylinder = FP), the gold standard locations (black dot = TP, red dot = FN), and the CT isosurface (gray) is shown. Columns 2–5 show representative oblique slices through these detections for the CT scan and MRI scans. [Color figure can be viewed at wileyonlinelibrary.com]

CT. A seed detected on MRI which was within 3 mm of a seed detected on CT was accepted as a pair of matching seeds and removed from the list of seeds that needed to be matched. The matching was ordered such that the pairs with the smallest distances to each other were accepted as matches first.

Any seed that was detected on MRI and matched on CT was classified as a true positive (TP) detection. Seeds detected on MRI that were not matched on CT were classified as false-positive (FP) detections. Finally, any seed that was detected on CT but not matched on MRI was classified as a false-negative (FN) detection.

Based on these classifications, we calculated the Dice similarity coefficient (DSC)[24] of the sets of detections on MRI and CT:

$$DSC = \frac{2TP}{2TP + FP + FN}$$

As a measure of the accuracy of the detected positions, we calculated the mean and standard deviation of the distance to the matched CT detection for the true positive detections.

All FPs and FNs were reviewed to assess the conditions in which the detection errors were made. Figure 4 shows examples of most of these conditions and how they appear on CT and MR scans. The false positives were classified in one of the following categories:

- *Incorrect automatic matching* [Fig. 4(b)]: In some cases, the distance between a correct detection on MR and CT was more than the 3-mm matching threshold. This category of false positive was chosen if clear seed artifacts were visible on the MR scan, while on the CT scan, a seed was detected nearby. When a one-to-one relationship was found between a FP and FN that were classified as incorrectly matched, we manually corrected the matching for these cases.
- *Near other seeds* [Fig. 4(c)]: In this case, the CT scan showed no seed at the location of the false positive, while one or more seeds were nearby.

- *Outside the prostate* [Fig. 4(d)]: This category of false positive was located outside of the segmented prostate and no seed was visible on the CT scan.
- *Unknown*: This was chosen if none of the conditions for the other categories were satisfied.

The false negatives were classified in on the following categories:

- *Incorrect automatic matching* [Fig. 4(b)]: This category of false negative was chosen if nearby a false positive was detected on the MR scan with clear seed artifacts visible.
- *Near other seeds* [Fig. 4(e)]: In this case, one or more seeds were visible on the CT scan near the false negative.
- *Part of an unspaced strand of seeds* [Fig. 4(f)]: This category of false negative was chosen if the seed was determined to be part of an unspaced strand of seeds based on the planning of the treatment.
- *Outside the region of interest*: In this case, the false negative was located outside the predetermined region of interest and was therefore unable to be detected.
- *Unknown*: This was chosen if none of the conditions for the other categories were satisfied.

The entire detection method was implemented in MATLAB (The Mathworks, Natick, MA, USA). Library generation took approximately 35 s per template, adding up to a total of just over 3 h for the complete library for each seed type. Seed detection took approximately 40 s per patient, varying slightly with the size of the region of interest and the number of seeds to be detected.

3. RESULTS

Figure 1 shows the magnetic field distortions induced by the presence of a brachytherapy seed in a static magnetic field. In Fig. 3(a), the artifacts resulting from these magnetic field distortions are visible in the magnitude images as well as the real and imaginary components of the complex-valued images. We observed a good correspondence between the simulated artifacts and the artifacts in actual MR scans. Even small differences in the artifacts due to the different compositions of the two types of brachytherapy seeds (Fig. 1) were simulated accurately. The examples in Fig. 3(a) show distinct patterns in the real and imaginary components of the signal that were not present in the magnitude of the signal. This suggests that in a gradient echo sequence, the complex-valued signal contains additional information regarding the position and orientation of the seeds, in comparison with the magnitude of the signal.

Figures 4(e) and 4(f) show examples of how the artifacts of multiple seeds can interact. In both the magnitude and the phase of the signal, the artifacts were more complicated than a simple combination of the artifacts of individual seeds. In the case of the unspaced strand of Best 2301 seeds [Fig. 4(f)], the seeds in the middle of the strand showed almost no artifacts.

Table I shows the detection results for the 25 patients, split by patients who were treated with the Best 2301 seeds (1A) and the selectSeed seeds (1B). We observed a false-negative rate of 4% for both types of seeds, a false discovery rate of 4% for the Best 2301 patients, and a false discovery rate of 5% for the selectSeed patients, where the false discovery rate is the percentage of all detections that were classified as false positives.

The true positive detections show a high spatial accuracy with regard to the registered CT locations. The mean distance was approximately 0.8 mm with 0.4 mm standard deviation, and in only two patients, the mean distance was higher than 1 mm (Table S1A and S1B).

Table II shows a summary of the classification of the detection errors. A total of four false positives and four false negatives did not satisfy any of the categories and were classified as unknown. False positives were most often found near other seeds: 72% for the Best 2301 patients and 61% for the selectSeed patients. For the Best 2301 patients, 82% of the false negatives were located in unspaced strands, which accounts for 42% of the total number of seeds in unspaced strands. For the selectSeed patients, the false negatives were approximately equally distributed between occurring near other seeds (42%) and in unspaced strands (37%).

TABLE I. Detection results per seed type. Reported values include the number of true positives (TP), false positives (FP), false negatives (FN), and the mean and standard deviation of the distance from the MR-only detections to the registered CT detections.

	Seeds implanted	Seeds counted on CT	TP	FP	FN	Dice overlap	Mean distance to CT (mm)	Standard deviation (mm)
Best 2301	1047	1046	1008	39	38	0.96	0.79	0.38
SelectSeed	510	501	482	28	19	0.95	0.83	0.46

TABLE II. Classification of the circumstances in which false positives (FP) and false negatives (FN) occurred per seed type. For each classification, the absolute number of occurrences and the percentage of the total number of false positives or false negatives is indicated.

	Total FP	Total FN	FP near other seeds	FP outside prostate	FN near other seeds	FN outside ROI	Total seeds in unspaced strands	FN in unspaced strands
Best 2301	39	38	28 (72%)	10 (26%)	1 (3%)	3 (8%)	73	31 (82% of FNs)
SelectSeed	28	19	17 (61%)	8 (29%)	8 (42%)	3 (16%)	42	7 (37% of FNs)

We corrected a total of seven seeds that were not automatically matched because they were outside of the 3-mm matching threshold. During the classification process, we also identified a total of nine cases (six FPs and three FNs) where an error in the CT gold standard was suspected. We made no corrections for these cases and selected the most appropriate classification, assuming the gold standard was correct.

Figure 5 shows the full detection results for one of the patients treated with the Best 2301 seeds (left) and for one of the patients treated with the selectSeed seeds (right). Both cases show a good correspondence between the detected seeds and the CT isosurface, in both position and orientation of the seeds.

Figure 6 shows the residual errors after regression for both seed types. This shows that most of the false-positive detections were associated with high errors and were found late in the detection process.

4. DISCUSSION

In this study, we applied a state-of-the-art MR-only seed localization method to in vivo scans of 25 patients who were treated with one of two types of brachytherapy seeds. Out of a total of 1557 seeds, we correctly localized 1490 seeds (96%). The total number of detection errors (false positives and false negatives) was 124, approximately 5 errors per patient on average. Although these numbers are promising, for postimplant dosimetry, the error rate is most likely still too high to be clinically applicable at this stage. The presented data allow a study that compares dosimetry based on MR and CT with MR-only dosimetry, which could determine what error rate is acceptable for clinical practice.

We have analyzed the circumstances in which the detection errors occurred. Here, we will discuss the sources of errors, to what degree they may be solved, and their impact on MR-only seed localization.

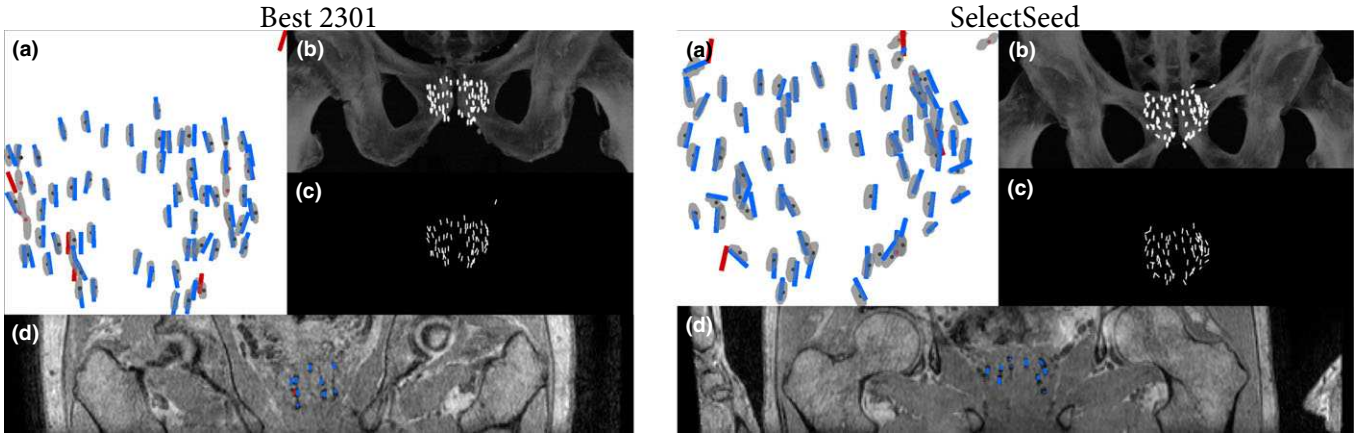

FIG. 5. Detection results for a Best 2301 patient (left) and selectSeed patient (right). Frontal view of localization and detection results (a) overlaid on a registered isosurface of the CT scan (gray). MR-only detections are shown as cylinders (blue = true positive, red = false positive). The CT detections are shown as dots (black = true positive, red = false negative). (b) A maximum intensity projection of the CT scan, and (c) a virtual maximum intensity projection of the detected seeds. (d) A coronal slice of the MR scan. [Color figure can be viewed at wileyonlinelibrary.com]

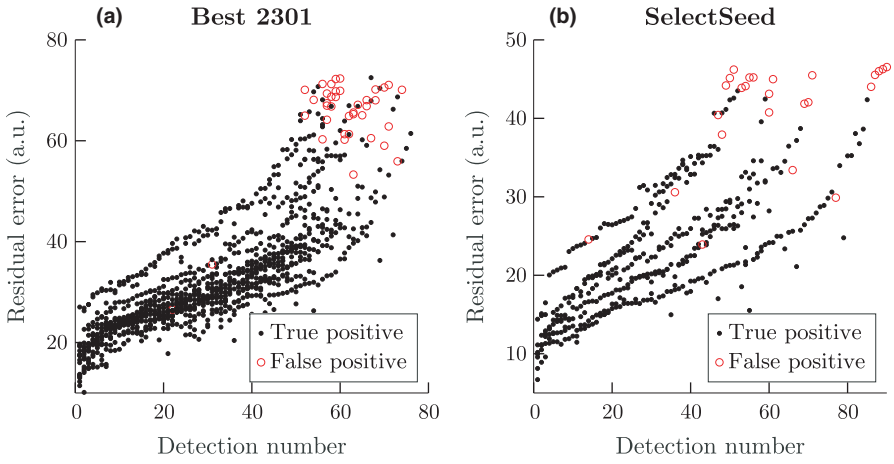

FIG. 6. Residual errors after regression analysis for the Best 2301 patients (a) and selectSeed patients (b). Each data point represents one MR-only seed detection, which was classified as either a true positive (black dot) or a false positive (red circle). The detection number is the order in which the seeds were detected per patient (i.e., the leftmost points were detected first). [Color figure can be viewed at wileyonlinelibrary.com]

The main source of errors we found was related to configurations of multiple seeds in close vicinity to each other. Because artifacts of multiple seeds near each other interact, localizing seeds based on these artifacts will be challenging. This interaction causes false negatives when the artifacts are no longer recognizable as the artifacts of individual seeds. We recognized a special case of this error in unspaced strands, i.e., seeds that were implanted close to each other by design. In the Best 2301 patients, a large amount of seeds placed in unspaced strand configurations were missed (31/73), which was the majority of all FNs (31/38). However, in the selectSeed patients, relatively few of the seeds in unspaced strands were missed (7/42), and these FNs formed a smaller fraction of the total number of FNs (7/19). This can be attributed to the composition of the selectSeed: the diamagnetic core and paramagnetic hull induce a complex magnetic field around the seed, which partially persists in unspaced strands, aiding detection. Because of its relatively simple, paramagnetic nature, Best 2301 seeds in an unspaced strand induce a field more consistent with a metal cylinder, where the field is only perturbed near the start and end of the strand, making detection of the seeds in the middle of the strand particularly challenging.

In the selectSeed patients, 8 of 19 FNs occurred in the vicinity of other seeds, while for the Best 2301 patients, this was only 1 of 38 FNs. This may be due to the fact that all selectSeed seeds are loose when they are implanted, can thus move more freely, and may therefore end up very close to each other (Fig. 5, right). However, most Best 2301 seeds are physically linked in strands that are more rigid and therefore much less likely to end up in such configurations (Fig. 5, left).

These results show that the type of brachytherapy seed and the implantation techniques clearly influenced the MR-only detection results. Optimization of such factors could be beneficial in a clinical implementation of MR-only seed localization and postimplant dosimetry. For example, suppose a treatment plan can be designed such that no unspaced strands of seeds are implanted. With such a plan, a majority of the FNs found in this study could have been avoided, which could make the proposed method competitive with CT-based seed localization. Alternatively, *a priori* information on the treatment plan could be used to improve upon our method. Under the assumption that seed migration is a rare occurrence, the seed locations are expected to closely match the treatment plan. This information could be useful in detecting false positives in locations where no seeds are expected, or to reconstruct strands of seeds with *a priori* information on the length and position of strands of seeds, which may be possible with methods previously applied to CT.[25]

Seeds outside of the region of interest were a minor source of false negatives. Two of six of these FNs were seeds that migrated to the seminal vesicles. The other four FNs were located just outside the ROI. Although extension of the ROI may have caused our method to find these seeds, it is important to note that extension of the ROI also increases the chance of false-positive detections occurring, especially if the ROI includes anatomies such as the rectum.

For both seed types, most false positives occurred in the vicinity of correctly detected seeds. Interaction between artifacts around multiple seeds is likely to partially match with some template in the library. False positives were also commonly found outside the prostate, where signal around the rectum and around small bleeds or calcifications can resemble artifacts around brachytherapy seeds. Most of these false positives were associated with high residual errors after regression (Fig. 6) and were, therefore, found late in the detection process. These false positives could be partially eliminated by stopping the detection algorithm when the matching errors are too high. Similarly, improving local matching with additional criteria may help in eliminating false positives that do not resemble brachytherapy seeds, for example, by locally analyzing the phase of the image with respect to the simulated phase around a seed. Such criteria may also be useful for human review and correction of the detection results; detections with high errors are likely to be false positives and could be flagged for a human operator to give it extra attention during review.

An important aspect of the proposed method is that it provides exact locations and orientations of the brachytherapy seeds. This is a clear advantage in comparison to methods that only provide visualization of seeds, for example, through positive contrast mechanisms.[16,17,19] In order to achieve this exact localization, we do require that certain prior knowledge is explicitly available. Most importantly, an exact model of the implanted brachytherapy seed must be available, including the magnetic susceptibility of the materials used in the seed. Furthermore, the exact scan parameters must be known, such as the k-space trajectory and the echo times. Other methods that do not require this prior knowledge could be easier to apply, in particular in cases where multiple types of seeds were implanted.

It is important to note that issues with seeds in close vicinity to each other are also likely to occur in other MR-only seed localization methods. Because the brachytherapy seed itself does not generate signal, information about the presence of a seed is always derived from tissue in the vicinity of the seed. Multiple seeds in close vicinity to each other will affect the same tissue, which then gives information about the presence of multiple seeds, but not about each seed individually. To resolve this issue, an MR-only localization method should be aware of the complex interactions occurring in such seed configurations. For example, the template libraries used in this study could be expanded with templates of a limited number of configurations of multiple seeds, based on prior knowledge of these specific configurations, such as the unspaced strands that caused most errors in the Best 2301 patients. However, due to computational limits, it will be impossible to include all possible configurations of multiple seeds in a method that relies on template matching to locate seeds. A certain number of false positives and false negatives in multiple seed configurations can, therefore, be expected, especially if these configurations occur because of

unpredictable phenomena, such as migration of seeds. An alternative approach could be to place positive contrast markers in strands of brachytherapy seeds to help localize these strands.[26] Our method could make use of these markers by including them in the simulation models. A downside of this approach is that it requires dedicated markers and is limited to stranded configurations of seeds.

In theory, any pulse sequence or contrast mechanism proposed in other studies could be combined with our localization approach, provided that the effects around the brachytherapy seeds can be accurately simulated in reasonable time. In this way, methods that yield positive contrast may be turned into localization methods. When applying the proposed method to other pulse sequences, it is important to remember that the effects around the brachytherapy seeds should be sufficiently large to allow reliable localization, but small enough such that interactions between multiple seeds are limited. Because off-resonance effects scale with field strength, artifacts around the seeds will be smaller at lower field strengths. This can be compensated by scanning with longer echo times or by using brachytherapy seeds with stronger magnetic susceptibilities. Conversely, at higher field strengths, artifacts will be larger, which allows scanning with shorter echo times, and could allow localization of brachytherapy seeds with weaker magnetic susceptibilities.

In this study, we assumed the only information on the number of seeds was the number of seeds that were implanted. In practice, seeds are occasionally lost; the number of seeds that were counted on CT during postimplant dosimetry showed that 10 seeds that were implanted were not found (Table I). This discrepancy resulted in 10 false positives. An appropriate stopping criterion would be required to deal with lost seeds, i.e., the method should only continue finding seeds when it is confident that the detections are real. A side-effect of such a stopping criterion would be that a failure to detect a seed no longer causes a false positive to be found in exchange.

The spatial accuracy of the true positive detections with respect to the CT detections was high, with an average error of 0.8 mm. The accuracy was probably limited by the fact that the detections were made at the MR resolution of 1.2 mm. It may be possible to improve on this by adapting the detection method to perform template matching at a subvoxel resolution.[27] Furthermore, the measured errors include the CT to MR registration errors due to nonrigid deformations. The high accuracy across the dataset of 25 patients indicates that the proposed method performed robustly in clinical conditions. Artifacts from patient motion and breathing were benign and did not appear to influence the seed localization.

Further analysis is required to establish the influence of using MR-only seed localization on postimplant dosimetry. Of particular importance is the influence of the absence of CT to MR registration errors on dosimetry. Another topic of interest is the influence of detection errors. It is possible that a single false positive or false negative detection may not have significant effects on the dose–volume calculations, because of the low dose of an individual seed. Finally, the information on seed orientation gained through MR-only seed localization may improve the accuracy of the dose calculations by allowing the use of anisotropic dose distributions.[28]

The proposed method is readily applicable in situations where fiducial markers have sufficient distance to each other, and therefore do not suffer from the challenges identified in this study. An example of such an application is the localization of gold fiducial markers for radiation therapy planning.[29]

5. CONCLUSION

This study shows that MR-only brachytherapy seed localization could be clinically feasible if the proposed method is made more robust with respect to seed configurations with many seeds close to each other. This may be achieved by including simulations of problematic seed configurations such as seeds in unspaced strands, or alternatively, by adapting seed implantation to help avoid such seed configurations. In addition, review by a human operator could help reduce false positives. Future research should establish whether dose distributions calculated based on a MR-only dosimetry workflow are of equal or better quality compared with the current clinical standard of using both CT and MR scans.

CONFLICTS OF INTEREST

The authors have no conflicts of interest to declare.

[a)]Author to whom correspondence should be addressed. Electronic mail: f.zijlstra@umcutrecht.nl; Telephone: +31 88 75 54633.

REFERENCES

1. Nag S, Ciezki JP, Cormack R, et al. Intraoperative planning and evaluation of permanent prostate brachytherapy: report of the American Brachytherapy Society. *Int J Radiat Oncol*. 2001;51:1422–1430.
2. Rivard MJ, Evans D-AR, Kay I. A technical evaluation of the Nucletron FIRST system: conformance of a remote afterloading brachytherapy seed implantation system to manufacturer specifications and AAPM Task Group report recommendations. *J Appl Clin Med Phys*. 2005; 6:22–50.
3. Radford Evans D-A, Meyer T, Angyalfi S, Husain S, Kay I, Dunscombe P. Enhanced efficiency and ergonomics of an intraoperative automated prostate brachytherapy delivery technique. *Brachytherapy*. 2007;6:254–257.
4. Taschereau R, Pouliot J, Roy J, Tremblay D. Seed misplacement and stabilizing needles in transperineal permanent prostate implants. *Radiother Oncol*. 2000;55:59–63.
5. Reed DR, Wallner KE, Merrick GS, et al. A prospective randomized comparison of stranded vs. loose 125I seeds for prostate brachytherapy. *Brachytherapy*. 2007;6:129–134.
6. Ash D, Flynn A, Battermann J, de Reijke T, Lavagnini P, Blank L. ESTRO/EAU/EORTC recommendations on permanent seed implantation for localized prostate cancer. *Radiother Oncol*. 2000;57:315–321.
7. Salembier C, Lavagnini P, Nickers P, et al. Tumour and target volumes in permanent prostate brachytherapy: a supplement to the ESTRO/EAU/EORTC recommendations on prostate brachytherapy. *Radiother Oncol*. 2007;83:3–10.
8. Barentsz JO, Richenberg J, Clements R, et al. ESUR prostate MR guidelines 2012. *Eur Radiol*. 2012;22:746–757.

9. Lim C, Malone SC, Avruch L, et al. Pictorial review. Magnetic resonance for radiotherapy management and treatment planning in prostatic carcinoma. *Br J Radiol*. 1054;2015:20150507.
10. Brown AP, Pugh TJ, Swanson DA, et al. Improving prostate brachytherapy quality assurance with MRI–CT fusion–based sector analysis in a phase II prospective trial of men with intermediate-risk prostate cancer. *Brachytherapy*. 2013;12:401–407.
11. De Brabandere M, Al-Qaisieh B, De Wever L, et al. CT- and MRI-based seed localization in postimplant evaluation after prostate brachytherapy. *Brachytherapy*. 2013;12:580–588.
12. Tanderup K, Viswanathan A, Kirisits C, Frank SJ. MRI-guided brachytherapy. *Semin Radiat Oncol*. 2014;24:181–191.
13. De Brabandere M, Kirisits C, Peeters R, Haustermans K, Van den Heuvel F. Accuracy of seed reconstruction in prostate postplanning studied with a CT- and MRI-compatible phantom. *Radiother Oncol*. 2006; 79:190–197.
14. Thomas SD, Wachowicz K, Fallone BG. MRI of prostate brachytherapy seeds at high field: a study in phantom. *Med Phys*. 2009;36:5228–5234.
15. Robertson AKH, Basran PS, Thomas SD, Wells D. CT, MR, and ultrasound image artifacts from prostate brachytherapy seed implants: the impact of seed size. *Med Phys*. 2012;39:2061–2068.
16. Kuo N, Lee J, Tempany C, Stuber M, Prince J. MRI-based prostate brachytherapy seed localization. *Proc IEEE Int Symp Biomed Imaging Nano Macro IEEE Int Symp Biomed Imaging*. 2010;2010:1397–1400.
17. Dong Y, Chang Z, Xie G, Whitehead G, Ji JX. Susceptibility-based positive contrast MRI of brachytherapy seeds. *Magn Reson Med*. 2015;74:716–726.
18. Wachowicz K, Thomas SD, Fallone BG. Characterization of the susceptibility artifact around a prostate brachytherapy seed in MRI. *Med Phys*. 2006;33:4459–4467.
19. Seevinck PR, de Leeuw H, Bos C, Bakker CJG. Highly localized positive contrast of small paramagnetic objects using 3D center-out radial sampling with off-resonance reception. *Magn Reson Med*. 2011;65:146–156.
20. Zijlstra F, Bouwman JG, Braškutė I, Viergever MA, Seevinck PR. Fast Fourier-based simulation of off-resonance artifacts in steady-state gradient echo MRI applied to metal object localization. *Magn Reson Med*. 2016. https://doi.org/10.1002/mrm.26556.
21. Kuglin CD, Hines DC. The Phase Correlation Image Alignment Method. In: Proc. of the IEEE Int. Conf. on Cybernetics and Society; 1975:163-165.
22. Bouwman JG, Bakker CJG. Alias subtraction more efficient than conventional zero-padding in the Fourier-based calculation of the susceptibility induced perturbation of the magnetic field in MR. *Magn Reson Med*. 2012;68:621–630.
23. Myronenko A, Song X. Point set registration: coherent point drift. *IEEE Trans Pattern Anal Mach Intell*. 2010;32:2262–2275.
24. Dice LR. Measures of the amount of ecologic association between species. *Ecology*. 1945;26:297–302.
25. Chng N, Spadinger I, Morris WJ, Usmani N, Salcudean S. Prostate brachytherapy postimplant dosimetry: automatic plan reconstruction of stranded implants. *Med Phys*. 2011;38:327–342.
26. Frank SJ, Stafford RJ, Bankson JA, et al. A novel MRI marker for prostate brachytherapy. *Int J Radiat Oncol*. 2008;71:5–8.
27. Alba A, Vigueras-Gomez JF, Arce-Santana ER, Aguilar-Ponce RM. Phase correlation with sub-pixel accuracy: a comparative study in 1D and 2D. *Comput Vis Image Underst*. 2015;137:76–87.
28. Collins Fekete C-A, Plamondon M, Martin A-G, Vigneault É, Verhaegen F, Beaulieu L. Quantifying the effect of seed orientation in postplanning dosimetry of low-dose-rate prostate brachytherapy. *Med Phys*. 2014;41:101704.
29. Ghose S, Mitra J, Rivest-Hénault D, et al. MRI-alone radiation therapy planning for prostate cancer: automatic fiducial marker detection. *Med Phys*. 2016;43:2218–2228.

SUPPORTING INFORMATION

Additional Supporting Information may be found online in the supporting information tab for this article.

Table S1. Detection results for Best 2301 patients. Reported values include the number of true positives (TP), false positives (FP), false negatives (FN), and the mean and standard deviation of the distance from the MR-only detections to the registered CT detections.